Influence of support morphology on the bonding of molecules to nanoparticles

Chi M. Yim[a], Chi L. Pang[a], Diego R. Hermoso[b], Coinneach M. Dover[a,1], Christopher A. Muryn[c], Francesco Maccherozzi[d], Sarnjeet S. Dhesi[d], Rubén Pérez[b,e], and Geoff Thornton[a,2]

[a]London Centre for Nanotechnology and Department of Chemistry, University College London, 17-19 Gordon Street, London, WC1H 0AH, UK

[b]Departamento de Fisica Teórica de la Materia Condensada, Módulo 05, Universidad Autonoma de Madrid, E-28049, Madrid, Spain

[c]School of Chemistry and Photon Science Institute, The University of Manchester, Oxford Road, Manchester, M13 9PL, UK

[d]Diamond Light Source, Harwell Science & Innovation Campus, Didcot, OX11 0DE, UK

[e]Condensed Matter Physics Center (IFIMAC), Universidad Autonoma de Madrid, E-28049, Madrid, Spain

[1]Present address: Scottish Microelectronics Centre, School of Engineering, The University of Edinburgh, Kings Buildings, Edinburgh, EH9 3JF, UK

[2]To whom correspondence should be addressed. E-mail: g.thornton@ucl.ac.uk.

KEYWORDS

Nanoparticle | carpet growth | surface strain | adsorption | STM | μ-NEXAFS

Abstract

Supported metal nanoparticles form the basis of heterogeneous catalysts. Above a certain nanoparticle size, it is generally assumed that adsorbates bond in an identical fashion as on a semi-infinite crystal. This assumption has allowed the database on metal single crystals accumulated over the past forty years to be used to model heterogeneous catalysts. Using a surface science approach to CO adsorption on supported Pd nanoparticles, we show that this assumption may be flawed. Near-edge X-ray absorption fine structure measurements, isolated to one nanoparticle, show that CO bonds upright on the nanoparticle top facets as expected from single crystal data. However, the CO lateral registry differs from the single crystal. Our calculations indicate that this is caused by the strain on the nanoparticle, induced by carpet growth across the substrate step-edges. This strain also weakens the CO–metal bond, which will reduce the energy barrier for catalytic reactions, including CO oxidation.

Significance

Supported metal nanoparticles often exhibit properties differing from those of their single crystal counterparts. There have been several suggested explanations for this, including quantum size effects, strong metal support interactions, and some interplay between facets. In this article, we show that the support morphology can also have a decisive role on the nanoparticle properties. Using scanning tunneling microscopy, we show that Pd nanocrystals formed across steps of a TiO_2 support have a curved top facet, where unusual adsorption behavior of CO is found. Calculations suggest that the different adsorption behavior arises from strain originating in the curved top facet. Our observations open the way for the tailoring of nanoparticle functionality by tuning the morphology of the support.

\body

Nanoparticles exhibit properties distinct from their bulk counterparts (1-3). For instance, semiconductor particles smaller than ~10 nm act as quantum dots (1-4) and oxide-supported gold nanoparticles are active for a variety of reactions including CO oxidation (5), water-gas-shift reaction (6), and epoxidation (7), whereas gold itself is not. Nanoclusters composed of ~10 atoms have been shown to be exceptionally catalytically active for some reactions on some metals (8, 9). When the particle size is reduced, the relative number of under-coordinated atoms at the edges and corners increase. The perimeter sites at the interface between the metal and the support also increase. All these sites have been shown to play a crucial role in some reactions (10, 11). Reducing the particle size can also lead to a decrease in the interatomic bond length in small metal clusters (12, 13), which in the case of Pd nanoparticles results in lower adsorption energies for both CO (14, 15) and O_2 (16), although such weakening of CO binding on the nanoparticle can also arise from other factors such as particle encapsulation of the nanoparticles by the support (17).

The role of the support in modifying nanoparticle properties has also been recognized. For instance, the strong-metal support interaction has been known for some time (2) and charge transfer either to or from the nanoparticles can lead to enhanced reactivity (18). More recently, it has come to light that the particle size itself may be governed by the interaction with the support (19). However, one effect that has not been discussed and yet should be present in any nanoparticle/support system is the influence of the support morphology such as steps.

Here, we investigate the role of the support morphology on the reactivity of metal nanoparticles using scanning tunneling microscopy (STM). As our test system we choose Pd nanoparticles (20, 21) supported on $TiO_2(110)$ (22) simply because much is known about both. The Pd nanoparticles were found to have curved top (111) facets that arise from 'carpet growth' of Pd across the step edges of $TiO_2(110)$ (Fig. 1*A*). While this carpet growth has been observed for graphene (23) and NaCl films (24), it has not been reported for metal nanoparticles. The effect of the curvature on the reactivity of the Pd nanoparticles was probed via the adsorption of CO molecules, CO on Pd(111) being a particularly well-understood system (25).

In Rose et al.'s scanning tunnelling microscopy (STM) study of Pd(111)-CO (25), it was observed that CO first fills threefold fcc-hollow sites, leading to a hollow (H)-($\sqrt{3}\times\sqrt{3}$)R30°-1CO overlayer at 0.33 monolayers (ML, 1 monolayer = 1.53×10^{15} molecules/cm^2), where 1CO indicates one CO molecule per primitive unit cell. As the coverage increases to 0.5 ML, CO also starts to fill bridge sites, so that bridge-bridge c(4×2)-2CO (BB) as well as hollow-hollow c(4×2)-2CO (HH) overlayers form. Above this coverage, CO fills a combination of atop and hollow sites, leading to an atop-hollow (2×2)-3CO overlayer at 0.75 ML. With the exception of the BB phase, we have previously observed all these overlayers on Pd nanoparticles supported on $TiO_2(110)$ (26). We also note that hollow site occupation of CO on the (111) top-facet of the alumina-supported Pd nanoparticles has been evidenced in some vibrational spectroscopy studies (27).

On the curved nanoparticle surfaces that we investigate here, we identify two additional CO phases that have not previously been observed either on Pd(111) (ref. 25) or $TiO_2(110)$-supported Pd nanoparticles (26). Based on density functional theory (DFT) calculations, we conclude that the new overlayers form due to the strain present above the underlying $TiO_2(110)$ steps.

Results and Discussions

The STM image shown in Fig. 1*A* was recorded from a $TiO_2(110)$ surface containing Pd nanocrystals ~20-30 nm wide. The top facets are hexagonal, indicative of (111) facets (28). According to the Wulff construction (28), the longer side facets are {111} and the shorter ones are {100}. We observe that one of the longer side facets is always parallel to the [001] direction of $TiO_2(110)$.

While some islands are found on terraces, many, like that in Fig. 1*A*, lie across the substrate step edges and we shall refer to these as step-islands. The step-island shown in Fig. 1*A* has a curved (111) top facet, as shown by the three color levels that comprise the top facet in the STM image. The topography of the top facet essentially follows that of the underlying $TiO_2(110)$ substrate: at the location of $TiO_2(110)$ step edges, the height of the Pd island changes. The three topographic levels can be clearly seen in the line profile of Fig. 1*B*. However, because the vertical separation between these levels is only ~100 pm and much lower than the step height of Pd(111) (224.5 pm), we conclude that the Pd curves over the $TiO_2(110)$ steps like a carpet, and we therefore refer to this as 'carpet growth' (23, 24).

The carpet growth is shown schematically in Fig. 1*C*. The $TiO_2(110)$ surface is represented as a rigid staircase with a step of 324.8 pm. On top of the $TiO_2(110)$ terraces, Pd atoms are stacked in (111) planes separated by 224.5 pm. This leads to a non-planar Pd(111) top facet with a vertical mismatch, between Pd layers originating from adjacent $TiO_2(110)$ layers, of 100.3 pm per $TiO_2(110)$ step. This matches closely with the line profile shown in Fig. 1*B*.

Figure 2*A* shows an STM image recorded from another Pd step-island covered with 0.5 ML CO. The top facet comprises a single Pd(111) terrace with individual spots in the image corresponding to CO molecules. The curvature of the island leads to a non-uniform background in the STM image that gives rise to a ~100 pm height variation across the entire (111) top facet, as shown in Fig. S1. Figure 2*B* shows a 'flattened' image, magnified from the square in Fig. 2*A*. In the flattened image, it is clear that several domains of CO co-exist on the surface.

The domain in the bottom left-hand side of the image has c(4×2) symmetry with the central spot of the unit cell exactly in the center and all spots with the same brightness. Of the possible c(4×2) structures that have CO in high symmetry positions, only the BB overlayer satisfies these conditions so this domain can be straightforwardly assigned as such. This BB overlayer has previously been observed in STM images of the native Pd(111) single crystals and the similarity between those STM images and that here is striking (25). The model for this overlayer is shown in the bottom left part of Fig. 2*D*.

In the top part of the image in Fig. 2*B*, there is an ordered array of brighter and darker spots. This is consistent with an atop-bridge (TB) overlayer where the CO molecules in atop positions appear brighter than those at bridge sites. To further confirm our assignment of this overlayer, we constructed a Pd(111) lattice on the bottom left part of the image based on the registration defined by the BB overlayer. This Pd(111) lattice is then extended to the top region of the image. Examination of the positions of the STM spots in the top part of Fig. 2*C* with respect to the constructed Pd(111) lattice confirms that the overlayer has TB site occupation, as shown in the model in Fig. 2*D*. Such a TB phase has not been reported on the native Pd(111) surface, despite extensive study (25).

Notice that in all our proposed models [and those by Rose et al. (25)] CO is assumed to bond with its molecular axis more-or-less normal to the (111) top facet, as has been observed on native Pd(111) (29). By employing X-ray photoemission electron microscopy (XPEEM), we tested this assumption through near-edge X-ray absorption fine structure (NEXAFS) measurements of a single nanoparticle, the first occasion that such a measurement has been reported. Taking so-called μ-NEXAFS data in this way eliminates averaging over an ensemble of nanoparticles. Detailed analysis of the μ-NEXAFS measurements is provided in the Supplementary Information. C K-edge μ-NEXAFS were taken from a Pd nanoparticle covered with 0.5 ML CO at a fixed incidence angle of 16° (30) with different polarization angles (β). Note that β = 90° (0°) corresponds to *s*- (*p*-) polarized light, the electric field vector of which lies perpendicular (parallel) to the plane of incidence. As shown in Fig. 3*A*, the CO π^* intensity signal (I) (centered at hν = 287 eV) decreases with decreasing β. By fitting the I vs β data (Fig. 3*B*) using equations adapted from Stöhr and Outka (31), we determined that the CO axis lies within 21.4° ± 7.0° of the surface normal. Previous C K-edge NEXAFS measurements of CO on the native Pd(111) surface reveal an upright bonding orientation (29). We attribute the discrepancy in the CO bond angle measured from the single crystal in ref. 25 and the nanoparticle data here to the signal contribution from CO adsorbed on side facets which are not included in the analysis. Hence, the μ-NEXAFS data indicate that there is some similarity in CO bonding to the nanoparticle and single crystal. Moreover, the data indicate that the nanoparticle is well-ordered.

Figure 4*A* shows an STM image recorded from another step-island also covered with 0.5 ML CO. The island has an average diameter and height of about 25 nm and 2.4 nm, respectively, as shown in Fig. S1. The top facet consists of a single terrace and is also curved, with a height variation of ~80 pm. The flattened image in Fig. 4*B* is expanded from the square in Fig. 4*A*. The overlayer has a c(4×2) symmetry as in Fig. 2 but with a zigzag motif that indicates that the central spot in the unit cell is offset from the center. Also because half of the spots appear brighter than the other half in the unit cell, this overlayer matches well with the atop-fcc hollow c(4×2)-2CO (TH) configuration shown in the model in Fig. 4*E*.

The subsequent image (Fig. 4*C*) displays a different CO configuration whilst retaining the same unit cell. As there was no indication of a change in the tip apex (32) between the two scans, and because some of the spots that are circled white in both images remain in the same positions, we believe that the CO overlayer changes its configuration going from Fig. 4*B* to 4*C*. This could be either a spontaneous change or due to some STM tip-initiated process.

The zigzag motif present in Fig. 4*B* is replaced with a rhombic motif in Fig. 4*C*. The open white circles in both images mark species that remain in the same position and we use them as registration marks. To determine the adsorption sites of CO in both overlayers, we superimpose the registration marks from Figs. 4*B*,*C* along with the colored circles that denote CO molecules. The resulting picture is shown in Fig. 4*D*. Half of the CO molecules remain in the same sites (those marked with dark-green circles) whereas the other half shift to the left, going from Fig. 4*B* to 4*C*.

To account for this, we examined the geometry of all possible transitions between c(4×2)-2CO overlayers with CO in high symmetry configurations: i.e. between HH, BB, TB, and TH. The transitions between TH and HH and between TB and BB can be discarded immediately as they do not lead to any change in the lateral pattern. Of the others, only the transition of TH to TB can explain the observed phase transition. These two models are shown in Fig. 4*E*. A region is shown where the two models overlap and the marks match perfectly with those in Fig. 4*D* (see the red dashed rectangles in Figs. 4*D*,*E*). As such, the overlayer in Fig. 4*B* is confirmed as TH and that in Fig. 4*C* can be assigned to TB. As with the TB structure observed here as well as in Fig. 2, the TH overlayer has also not been observed on native Pd(111) (25), although CO occupancy of the atop site has been detected at higher coverages: between 0.6 and 0.75 ML (33).

At a coverage of 0.5 ML on native Pd(111), only the formation of c(4×2)-2CO structures with HH and BB site occupations have been reported (25) whereas on the curved Pd(111) top facets here, we also observe TB and TH structures. To account for differences in properties between nanoparticles and their corresponding extended surfaces, the following factors are usually invoked: particle size effects, chemical composition, and particle-support interactions. First, we can rule out particle size effects. This is because the Pd particle size of 20-30 nm probed here already reaches the bulk limit of Pd(111) as reflected in temperature programmed desorption (TPD) and single-crystal adsorption calorimetry (SCAC) measurements of adsorbed CO. Naturally, our results therefore have no implications on this controversial issue (15). As for the chemical composition, our X-ray photoelectron spectroscopy (XPS) data suggest that the nanoparticles are composed of only Pd. XPS cannot exclude the presence of a small amount of Ti or H. However, we have imaged the nanoparticles with atomic resolution and they appear as clean Pd(111) top facets, whereas encapsulation with TiO_x leads to zigzag or pinwheel structures (20). Also, due to the particle growth method employed, we expect that any H present will reside in the subsurface of the nanoparticles (34), and therefore will not cause any change to the adsorption behavior of CO on the nanoparticle top facet (35). On this basis, we also rule out the chemical composition as a factor and consider instead the particle-support interaction. To form a carpet, the Pd lattice elongates (tensile strain) in the direction across the step-edge, and in order to minimize the elastic energy cost, the lattice shrinks (compressed strain) in the orthogonal direction. We suggest that this strain modifies the CO-Pd(111) adsorption behavior.

To test this idea, we employ DFT calculations (see Calculation Details in SI Methods) to study the effect of strain on the stability of different c(4×2)-2CO overlayers on Pd(111). In the calculations, tensile strain ($\varepsilon_s > 0$) is modeled by elongation along $\left[\bar{1}01\right]$ (see Fig. 5*B*) together with compression along $\left[\bar{1}2\bar{1}\right]$ and *vice versa* for compressive strain ($\varepsilon_s < 0$). As shown in Fig. 5*A*, with no surface stress, the HH overlayer has the lowest energy, followed by BB (ΔE = 0.053 eV/molecule). As for the TB overlayer, this is unstable in the computation and relaxes to HH. Although application of the surface strain does not alter this hierarchy of stability, it does have a significant impact on the formation energies of the overlayers. In particular, under both tensile and compressive strains, one can see that the gap in the formation energies of the different overlayers becomes smaller (the gap between BB and HH decreases from 0.053 eV at $\varepsilon_s = 0$ to 0.025 eV at $\varepsilon_s = -0.04$ and to 0.029 eV at $\varepsilon_s = +0.1$). The reduction of the energy gap between different phases arises from a reduction in intermolecular repulsion between CO as the lattice expands along one direction and compresses along another. Note that at $\varepsilon_s = +0.04$, the TB overlayer relaxes to the more stable, geometrically similar, TH configuration.

These calculations indicate that the TB configuration becomes more likely when the Pd(111) lattice is strained. Nevertheless, while the tensile surface strain can lower the energy gap between the TB and HH structures, our calculations still predict that the HH overlayer is the most stable. However, it is well known that DFT *under*-estimates the cost of breaking one of the bonds from a triply-bonded CO molecule (36). Given that CO in an atop site is close to being doubly-bonded and CO in a hollow site is close to being singly-bonded, it follows that DFT *over*-estimates the strength of CO adsorption in threefold hollow sites (36). This explains the discrepancies found between experiment and calculation, where DFT fails to predict the experimentally observed atop-site occupation at low coverage for CO adsorption on both native Pt(111) and Rh(111) (36, 37). To reduce or solve completely such site preference discrepancies in DFT, one can employ the newly-developed van der Waals-density functional (vdW-DF) of nonlocal correction as shown by Lazić et al. (38). In addition to this, recent calculations based on many-body perturbation theory (MBPT), including the exact exchange and correlation energy using the random phase approximation (RPA), correctly predict the atop site to be the lowest energy adsorption configuration for Pt(111) and Rh(111) (39). These same calculations show a significant reduction (more than 50%) in the energy difference between the hollow and atop sites for Pd(111) (from ~0.75 eV using the PBEsol XC functional to ~0.37 eV using RPA).

Calculations using RPA (39) for the current system are not feasible. Instead, we evaluate how much the vdW functional overestimates the adsorption energy of CO at the hollow site by calculating the difference in the adsorption energies of CO at the atop and fcc hollow sites in a (2×2) unit cell using two other functionals: PBE and PBEsol, and compared our results to those obtained using RPA (39). To check for consistency with the PBE functional we also calculated the adsorption energy gap of CO at both sites in a smaller, ($\sqrt{3}\times\sqrt{3}$) unit cell. Under the same PBE functional, both unit cells yield the same adsorption energy gap of $\Delta E_{fcc\text{-}atop} = -0.59$ eV. In addition, $\Delta E_{fcc\text{-}atop}$ obtained using the PBEsol functional (-0.72 eV) here is very close to that obtained using the same PBEsol functional (-0.73 eV) in the work of Schimka et al. (39). This validates the compatibility between our calculations and those in ref. 39. By comparing the $\Delta E_{fcc\text{-}atop}$ value obtained using the vdW functional (-0.62 eV) here to that obtained using the RPA in ref. 39, we deduce that the vdW functional employed here overestimates the adsorption energy of CO at the hollow site by 0.25 eV.

To take this into account, we have added an extra curve (orange) in Fig. 5*A*, which is identical to the original TB curve (red), but has its formation energies in all surface strain conditions lowered by 0.25 eV. This new curve shows that under tensile strain, TB can be competitive with HH and even have a lower formation energy (above $\varepsilon_s = +0.04$).

Surface strain, which has been shown to alter the reactivity of metal substrates (40), can play a vital role in the adsorption of molecules on nanoparticles. For example, Peter et al. (15) point out that Pd nanoparticles less than 8 nm in diameter are compressively strained, and this leads to weaker CO adsorption. However, unlike the strain that arises from the particle size effect (15) or that from lattice mismatch, which is periodic and incremental in nature, the strain that is caused by particle growth across the substrate step edges is highly localized and abrupt. It may therefore have a more profound effect on gas adsorption in the vicinity of the underlying substrate steps or other lateral discontinuities.

Apart from nucleating the growth of additional phases, we also have evidence that the curved areas of the top facets can separate different CO domains. Figure 6*A* shows an STM image recorded from another Pd step-island. The top facet consists of a single terrace and the island was covered with 0.5 ML CO. Most of the facet is covered with HH domains. However, there is a crescent-shaped region that is heavily sloped on both sides. It is apparent from the flattened image in Fig. 6*B* that this region does not contain ordered CO. Instead, as a direct consequence of the underlying TiO_2 steps, the region is either devoid of CO or contains disordered CO that is highly mobile. This suggests that different (local) morphology can lead to different adsorption properties and therefore reactivity on some parts of the nanoparticle.

It is very likely that the carpet growth observed here will also occur in other nanostructured systems comprising an interface between two materials (3). Not only will this support morphology effect have a critical impact on the rate of chemical reactions (3), it also offers the opportunity for tuning reactivity by designing the nanoparticle/substrate interface.

Methods

Scanning tunneling microscopy (STM). STM experiments were performed using an *Omicron GmbH* low temperature ultrahigh vacuum (UHV) STM. $TiO_2(110)$ samples (*Pi-Kem*) were prepared by Ar^+ ion sputtering and annealing to ~1000 K, forming an 'as-prepared' sample (22). Nanoparticles were formed by depositing Pd (*Advent Research Materials*, 99.95 %) onto such as-prepared samples held at ~700 K. The doser consisted of Pd wire wrapped around a W filament. CO was mainly dosed *in-situ*, although in some cases this was also done *ex-situ*. *In-situ* dosing employed a directional doser placed ~50 mm from the STM stage, with the sample held in the stage at 124-150 K. *Ex-situ* dosing was performed with the sample at room temperature via a leak-valve in the preparation chamber; after dosing, the sample was moved to the STM stage for imaging at 78 K. XPS was used to confirm the surfaces were free from contamination after CO dosing.

Synchrotron radiation measurements. Spatially-resolved NEXAFS (μ-NEXAFS) measurements were performed at the Diamond Light Source, using the I06-Nanoscience soft X-ray beamline (30). The end-station is an Elmitec LEEM III spectroscopic photoemission and low energy electron microscope (SPELEEM). In this instrument, X-ray photoemission as well as X-ray absorption in secondary electron yield mode can be performed with a spatial resolution of ~50 nm and a photon energy resolution of ~300 meV in imaging mode.

Rutile $TiO_2(110)$ samples were prepared in the same way as in the STM experiments, with surface cleanliness checked using Auger electron spectroscopy (AES). Pd was deposited from a Mo crucible heated by electron bombardment (*Omicron GmbH EFM3*) onto a $TiO_2(110)$ sample held at 850 K. In LEED, the surface exhibited sharp Pd(111)-(1×1) diffraction spots, indicating that the Pd nanoparticles have well-ordered top facets. CO was dosed *in-situ* by filling the analysis chamber. Secondary electron yield carbon K-edge (hv = 285-295 eV) μ-NEXAFS measurements were performed to determine the bond orientation of CO on individual Pd nanoparticles. Normalization involves subtraction of the spectra recorded on and off the CO-covered Pd nanoparticles. The photon energy around the carbon K-edge was calibrated using the π* resonance peak of a graphite sample (41).

ACKNOWLEDGEMENTS

G.T. acknowledges useful discussions with Prof. Günther Rupprechter. This work was supported by EPSRC (UK) EP/G067384, European Cooperation in Science and Technology Action CM1104, The Royal Society and European Research Council Advanced Grant ENERGYSURF (G.T.). D.R.H. and R.P. acknowledge the support of the Project MAT2011-023627(Ministry of Economy and Competitiveness, Spain) and the computer time provided by the Spanish Supercomputing Network at the Barcelona Supercomputing Center (BSC).

Author Contributions:

G.T. designed research; C.M.Y. and C.L.P. carried out STM measurements and analyzed the data; C.M.D., C.M.Y., C.A.M., F.M. and S.S.D. performed X-ray absorption and NEXAFS measurements, with C.M.D. and C.M.Y. analyzing the data; D.R.H. and R.P. performed the theoretical calculations; C.M.Y., C.L.P. and G.T. wrote the manuscript and the supporting information with input from all authors. All authors participated in discussing the data.

References

1. Zhdanov VP, Kasemo B (2000) Simulations of the reaction kinetics on nanometer supported catalyst particles. *Surf Sci Rep* 39:25–104.
2. Tauster SJ (1987) Strong metal-support interactions. *Acc Chem Res* 20:389–394.
3. Jackson SD, Hargreaves JSJ (2008) *Metal Oxide Catalysis* (Wiley, WeinHeim).
4. Robel I, Kuno M, Kamat PV (2007) Size-dependent electron injection from excited CdSe quantum dots into TiO_2 nanoparticles. *J Am Chem Soc* 129:4136–4137.
5. Haruta M et al. (1993) Low-temperature oxidation of CO over gold supported on TiO_2, α-Fe_2O_3, and Co_3O_4. *J Catal* 144:175–192.
6. Tao F, Ma Z (2013) Water-gas shift on gold catalysts: catalyst systems and fundamental studies. *Phys Chem Chem Phys* 15:15260–15270.
7. Choudhary VR, Dumbre DK (2009) Supported Nano-Gold Catalysts for Epoxidation of Styrene and Oxidation of Benzyl Alcohol to Benzaldehyde. *Top Catal* 52:1677–1687.
8. Kaden WE, Wu T, Kunkel WA, Anderson SL (2009) Electronic structure controls reactivity of size-selected Pd clusters adsorbed on TiO_2 surfaces. *Science* 326:826–829.
9. Herzing AA, Kiely CJ, Carley AF, Landon P, Hutchings GJ (2008) Identification of active gold nanoclusters on iron oxide supports for CO oxidation. *Science* 321:1331–1335.

10. Ludwig W, Savara A, Schauermann S, Freund H-J (2010) Role of low-coordinated surface sites in olefin hydrogenation: a molecular beam study on Pd nanoparticles and Pd(111). *ChemPhysChem* 11:2319–2322.

11. Green IX, Tang W, Neurock M, Yates JT (2011) Spectroscopic observation of dual catalytic sites during oxidation of CO on a Au/TiO_2 catalyst. *Science* 333:736–739.

12. Nepijko SA et al. (1999) Structural investigation of palladium clusters on gamma-Al_2O_3(111)/NiAl(110) with transmission electron microscopy. *Langmuir* 15:5309–5313.

13. Yudanov IV, Metzner M, Genest A, Rösch N (2008) Size-dependence of adsorption properties of metal nanoparticles: a density functional study on palladium nanoclusters. *J Phys Chem C*112:20269–20275.

14. Fischer-Wolfarth J-H et al. (2010) Particle-size dependent heats of adsorption of CO on supported Pd nanoparticles as measured with a single-crystal microcalorimeter. *Phys Rev B*81:241416.

15. Peter M, Adamovsky S, Flores Camacho JM, Schauermann S (2013) Energetics of elementary reaction steps relevant for CO oxidation: CO and O_2 adsorption on model Pd nanoparticles and Pd(111). *Faraday Discuss* 162:341.

16. Peter M et al. (2013) Trends in der Bindungsstärke von Oberflächenspezies auf Nanopartikeln: Wie verändert sich die Adsorptionsenergie mit der Partikelgröße? *Angew Chem* 125:5282–5287.

17. Campbell CT, Sellers JRV (2013) Anchored metal nanoparticles: Effects of support and size on their energy, sintering resistance and reactivity. *Faraday Discuss* 162:9–30.

18. Yoon B (2005) Charging effects on bonding and catalyzed oxidation of CO on Au_8 clusters on MgO. *Science* 307:403–407.

19. Farmer JA, Campbell CT (2010) Ceria maintains smaller metal catalyst particles by strong metal-support bonding. *Science* 329:933–936.

20. Bowker M et al. (2005) Model catalyst studies of the strong metal–support interaction: surface structure identified by STM on Pd nanoparticles on TiO_2(110). *J Catal* 234:172–181.

21. Humphrey DS et al. (2009) Self-assembled metallic nanowires on a dielectric support: Pd on rutile TiO_2(110). *Nano Lett* 9:155–159.

22. Pang CL, Lindsay R, Thornton G (2013) Structure of clean and adsorbate-covered single-crystal rutile TiO_2 surfaces. *Chem Rev* 113:3887–3948.

23. Sutter PW, Flege JI, Sutter EA (2008) Epitaxial graphene on ruthenium. *Nat Mater* 7:406–411.

24. Matthaei F et al. (2012) Coulomb attraction during the carpet growth mode of NaCl. *J Phys: Condens Matter* 24:354006.

25. Rose MK et al. (2002) Ordered structures of CO on Pd (111) studied by STM. *Surf Sci* 512:48–60.

26. Yim CM et al. (2013) CO and O overlayers on Pd nanocrystals supported on TiO_2(110). *Faraday Discuss* 162:191.

27. Yudanov IV et al. (2003) CO adsorption on Pd nanoparticles: density functional and vibrational spectroscopy studies. *J Phys Chem B* 107:255–264.

28. Højrup-Hansen K et al. (1999) Palladium nanocrystals on Al_2O_3: structure and adhesion energy. *Phys Rev Lett* 83:4120.

29. Knight MJ et al. (2008) A structural study of a C_3H_3 species coadsorbed with CO on Pd(111). *Surf Sci* 602:2743–2751.

30. Dhesi SS et al. (2010) The Nanoscience Beamline (I06) at Diamond Light Source. *AIP Conf Proc* 1234:311–314.

31. Stöhr J, Outka DA (1987) Determination of molecular orientations on surfaces from the angular dependence of near-edge X-ray-absorption fine-structure spectra. *Phys Rev B* 36:7891.

32. Sánchez-Sánchez C et al. (2010) Understanding atomic-resolved STM images on TiO_2(110)-(1×1) surface by DFT calculations. *Nanotechnology* 21:405702.

33. Rupprechter G (2007) Sum frequency generation and polarization–modulation infrared reflection absorption spectroscopy of functioning model catalysts from ultrahigh vacuum to ambient pressure. *Adv Catal* 51:133–263.

34. Mitsui T, Rose MK, Fomin E, Ogletree DF, Salmeron M (2002) Coadsorption and interactions of O and H on Pd (111). *Surf Sci* 511:259–266.

35. Morkel M, Rupprechter G, Freund H-J (2003) Ultrahigh vacuum and high-pressure coadsorption of CO and H_2 on Pd (111): A combined SFG, TDS, and LEED study. *J Chem Phys* 119:10853–10866.

36. Grinberg I, Yourdshahyan Y, Rappe AM (2002) CO on Pt(111) puzzle: a possible solution. *J Chem Phys* 117:2264.

37. Köhler L, Kresse G (2004) Density functional study of CO on Rh(111). *Phys Rev B* 70:165405.

38. Lazić P et al. (2010) Density functional theory with nonlocal correlation: a key to the solution of the CO adsorption puzzle. *Phys Rev B* 81:045401.

39. Schimka L et al. (2010) Accurate surface and adsorption energies from many-body perturbation theory. *Nat Mater* 9:741–744.

40. Mavrikakis M, Hammer B, Nørskov JK (1998) Effect of strain on the reactivity of metal surfaces. *Phys Rev Lett* 81:2819.

41. Endo O et al. (2011) Orientation of n-alkane in thin films on graphite (0001) studied using C K-NEXAFS. *J Electron Spectrosc Relat Phenom* 184:257–260.

42. Kresse G, Furthmüller J (1996) Efficiency of ab-initio total energy calculations for metals and semiconductors using a plane-wave basis set. *Comput Mater Sci* 6:15–50.

43. Kresse G, Furthmüller J (1996) Efficient iterative schemes for ab initio total-energy calculations using a plane-wave basis set. *Phys Rev, B Condens Matter* 54:11169–11186.

44. Klimeš J, Bowler DR, Michaelides A (2011) Van der Waals density functionals applied to solids. *Phys Rev B* 83:195131.

45. Román-Pérez G, Soler J (2009) Efficient implementation of a Van der Waals density functional: application to double-wall carbon nanotubes. *Phys Rev Lett* 103:096102.

Figure

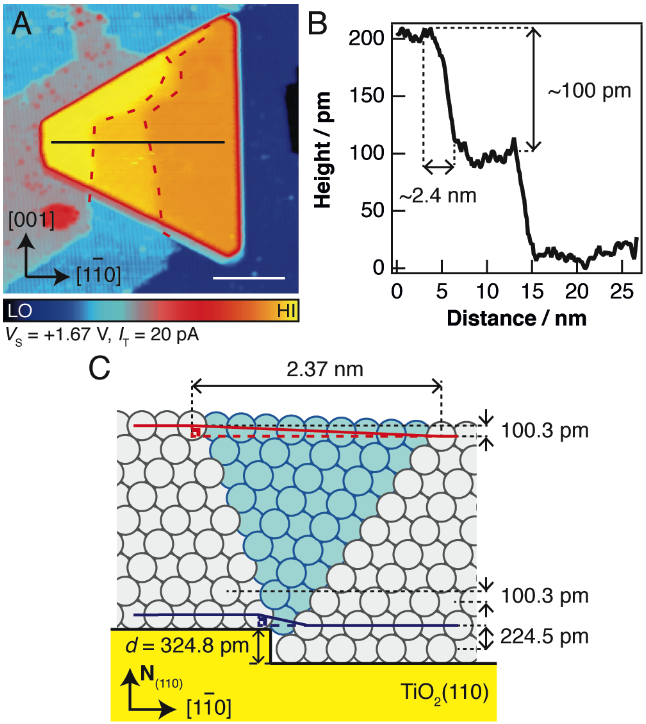

Fig. 1. Pd step-island with a curved (111) top facet formed by 'carpet-growth' across the TiO_2(110) step-edge. (*A*) 45 × 45 nm^2 STM image recorded from a Pd nanoparticle spanning two step edges of the underlying TiO_2 substrate. The nanoparticle has a measured diameter (*d*) of about 30 nm and a height (*h*) of 1.9 nm. Red dashed lines roughly mark the locations of the step edges lying beneath the nanoparticle. The nanoparticle and the TiO_2(110) substrate renditions are composed from two versions of the same image. One has background subtraction optimized for the substrate and the other for the Pd nanoparticle. This was necessary in order to visualize the substrate and the island together with high contrast. The color bar is identical in both components of the image and has a range of 2.23 nm. The scale bar is 11 nm. (*B*) Line profile taken from the black line in *A*. (*C*) Schematic showing a cross-section of a Pd nanocrystal spanning two adjacent TiO_2(110) terraces. Pd(111) stacks with an interlayer spacing of 224.5 pm are placed on top of both TiO_2(110) terraces leading to a vertical mismatch of 100.3 pm between Pd(111) layers that

originate from different terraces. This vertical mismatch is accommodated by formation of a ‘carpet’ region highlighted in blue.

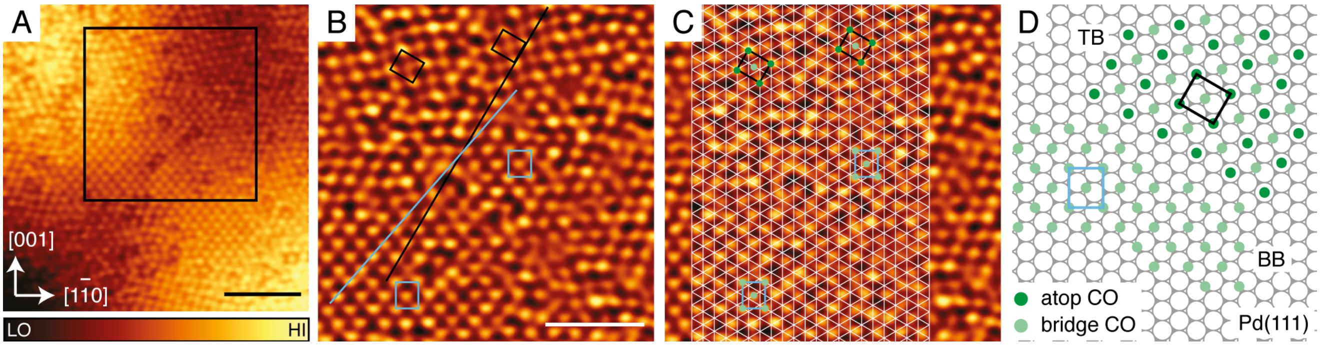

Fig. 2. c(4×2)-2CO structures with atop-bridge (TB) and bridge-bridge (BB) site occupations on a curved Pd(111) top facet. (*A*) STM image (V_S = 0.6 V, I_T = 0.1 nA, 12 × 12 nm^2, 78 K) recorded from a Pd step-island (*d* = 43 nm, *h* = 4.8 nm) covered with 0.5 ML CO. The color bar has a range of 77 pm. The scale bar is 3 nm. An image of the entire island is shown in Fig. S1. (*B*) Image magnified (6.9 × 6.9 nm^2) from the square marked in *A* and flattened by applying a band-pass filter. Two separate BB regions are highlighted with light blue unit cells and two separate TB regions are marked with black unit cells. The light-blue (black) guideline is aligned to spots from the BB (TB) domain and is exactly 49.1º (60º) from the horizontal as would be expected from the ideal structure. Note that the excellent fit of these angles indicates an image largely free from distortion as required for reliable site assignment. The scale bar is 2 nm. (*C*), As *B*, with a perfect hexagonal grid superimposed on part of the image. The positions of Pd atoms are marked by interstices in the grid. The registration of the STM spots with the grid confirms the presence of both BB and TB overlayers. We superimpose two well-separated unit cells each for the BB and TB overlayers which show the validity of the Pd(111) grid. Some CO in atop and bridge positions are marked dark- and light-green, respectively. (*D*) Ball model showing TB and BB configurations in the top right and bottom left, respectively.

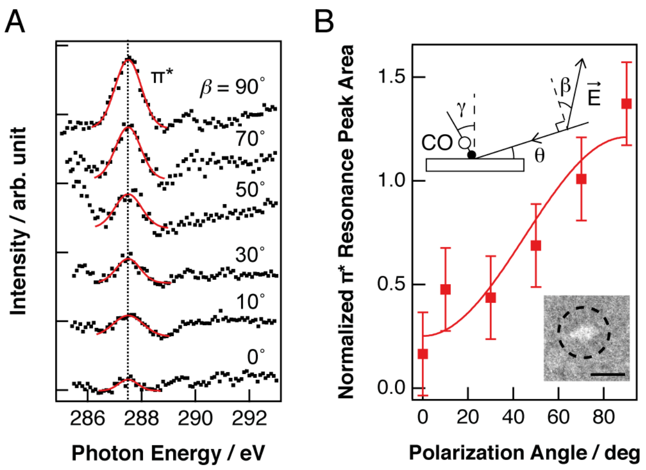

Fig. 3. Bonding orientation of CO on a single Pd nanocrystal supported on $TiO_2(110)$. (*A*) Normalized C K-edge NEXAFS spectra recorded at different polarization angles (*β*) from a Pd nanoparticle [inset of *B*] covered with 0.5 ML CO. (*B*) Integrated intensity of the CO π* resonance peak as a function of *β*. Markers are the experimental data and the solid line is the numerical fit to the experimental data. The numerical fit reveals an apparent bond angle γ of 21.4° ± 7.0°. (*Inset*) 5 × 5 μm^2 XPEEM image of a Pd nanoparticle supported on $TiO_2(110)$. The image was recorded at photon energy of 430 eV. The scale bar is 2 μm. The particle has a measured diameter of 1.5 μm.

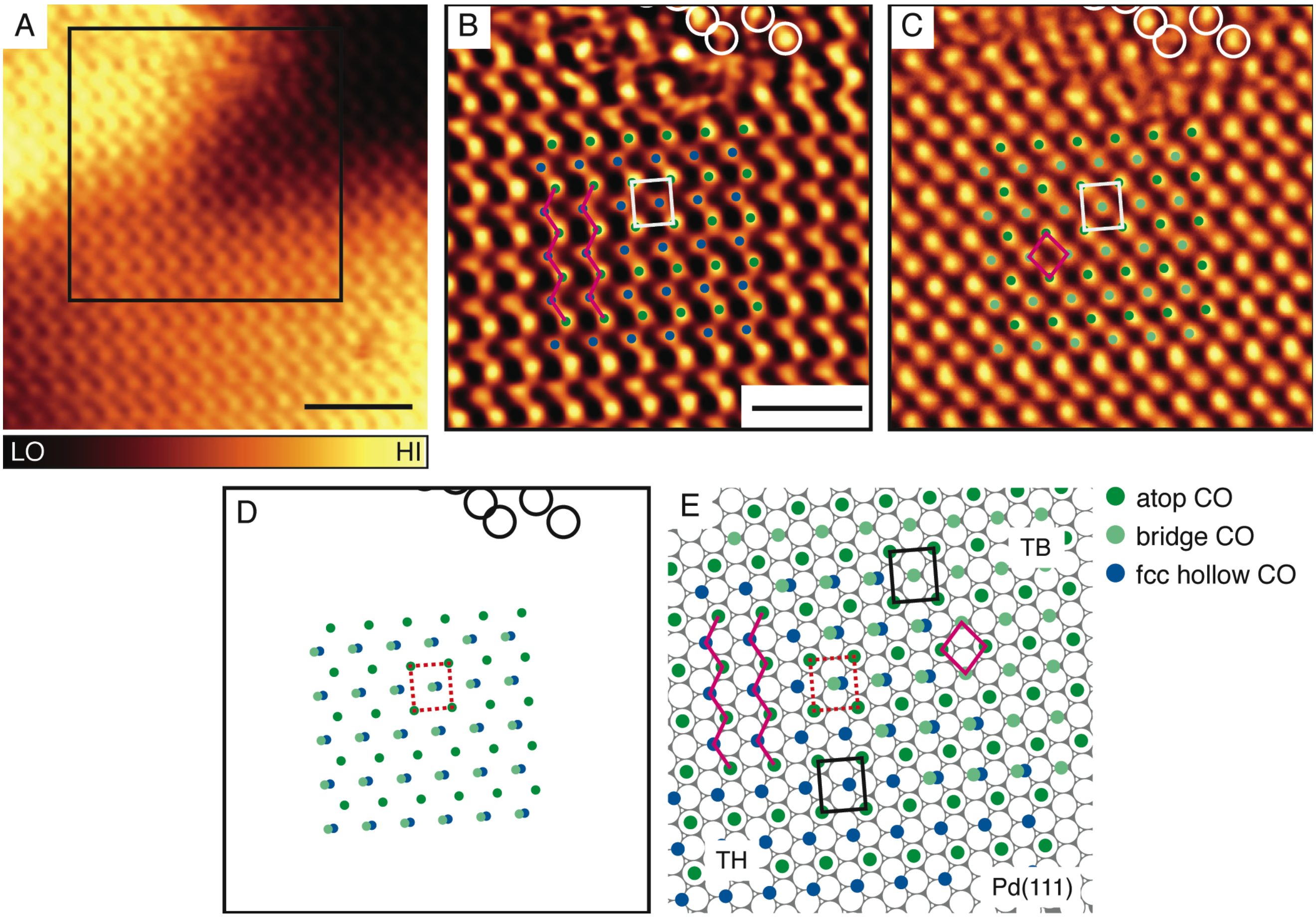

Fig. 4. c(4×2)-2CO structure with atop-fcc hollow (TH) site occupation on a Pd(111) top facet. (*A*) STM image (V_S = 0.8 V, I_T = 80 pA, 7.9 × 7.9 nm^2, 124 K) recorded from a Pd step-island (d = 24.6 nm, h = 2.4 nm) covered with 0.5 ML of CO. The color bar has a range of 67 pm. An image showing the entire step-island can be seen in Fig. S1. The scale bar is 2 nm. (*B*) Magnified area (5.04 × 5.04 nm^2) from the square in *A*, flattened by applying a band-pass filter. The scale bar is 1.3 nm. (*C*) An image recorded (V_S = 0.8 V, I_T = 80 pA, 5.04 × 5.04 nm^2) after acquisition of that in *B*, also band-pass filtered. In *B* and *C*, some spots that do not change position between the two images are marked with white open. The c(4×2)-2CO unit cell is indicated with a white square and dark-green circles mark atop positions. Additionally, in *B*, blue circles mark fcc hollow sites and in *C*, light-green circles indicate bridge sites. This leads to a zigzag motif in *B* and a rhombic motif in *C*, highlighted pink. (*D*) The

marks from *B* and *C* are overlaid so that the registration marks (shown in black here) are exactly aligned. While the atop CO remain on the same sites going from *B* to *C*, the fcc-hollow CO molecules shift to the bridge site. (*E*) Ball model showing TH and BB domains with the same color-coding as *B* and *C*. Between the two domains, we allow the models to overlap and a red dashed rectangle highlights a region that can be directly compared with the red dashed rectangle in *D*.

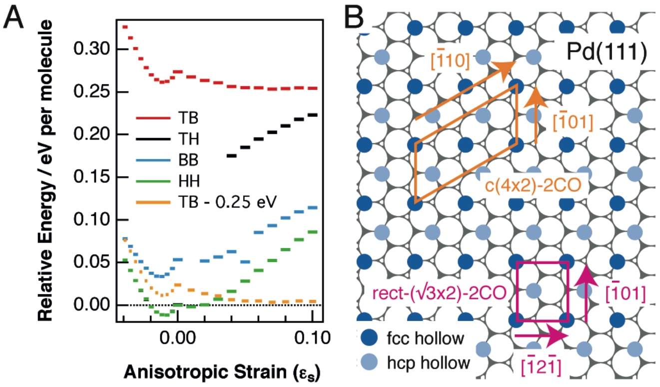

Fig. 5. Strain dependence of the stability of different c(4×2)-2CO configurations on Pd(111). (*A*) Graph showing the calculated (DFT+vdW) stability between different c(4×2)-2CO configurations and their dependence on anisotropic surface strain: at $\varepsilon_s > 0$ ($\varepsilon_s < 0$), the lattice is elongated (compressed) along $[\bar{1}01]$ and compressed (elongated) along $[\bar{1}2\bar{1}]$. Three different c(4×2)-2CO unit cells, namely TB, BB, and HH are initially considered. In the calculations, the CO molecules are allowed to relax and the TB configuration (red) stabilizes to the HH (green) configuration for all compressive strains ($\varepsilon_s < 0$) and for low tensile strains ($0 < \varepsilon_s < +0.04$). High tensile strain ($\varepsilon_s > +0.04$) stabilizes the TH structure (black). Orange lines correspond to the TB configuration lowered by 0.25 eV for all ε_s. (*B*) Ball model showing the c(4×2)-2CO unit cell (in the HH configuration) and equivalent primitive *rect*-$\left(\sqrt{3}\times 2\right)$ unit cell in relation to Pd(111) azimuths.

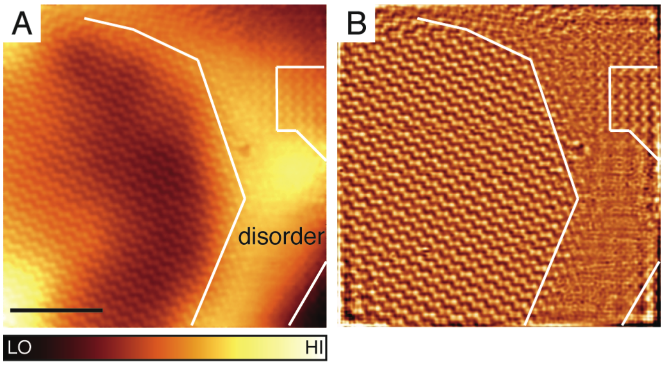

Fig. 6. Formation of an adsorption domain boundary on a curved Pd(111) top facet. (*A*) STM image (V_S = 1 V, I_T = 20 pA, 13.8 × 13.8 nm^2, 150 K) recorded from a Pd step-island (*d* = 24.6 nm, *h* = 2.4 nm) covered with 0.5 ML of CO. The color bar has a range of 161 pm. The scale bar is 4 nm. An image showing the entire step-island can be seen in Fig. S1. (*B*) As *A*, but flattened by applying a band-pass filter. In *A* and *B*, the white lines mark the region that is sloped.